An Improved Volume of Fluid Method for Two-Phase Flow Computations on Collocated Grid System

Dong-Liang Sun

Yong-Ping Yang

Jin-Liang Xu[1]
e-mail: xjl@ncepu.edu.cn

Beijing Key Laboratory of New and Renewable Energy,
North China Electric Power University,
Beijing 102206, P.R. China

Wen-Quan Tao
School of Power and Energy Engineering,
Xi'an Jiaotong University,
Xi'an, Shaanxi 710049, P.R. China

An improved volume of fluid method called the accurate density and viscosity volume of fluid (ADV-VOF) method is proposed to solve two-phase flow problems. The method has the following features: (1) All operations are performed on a collocated grid system. (2) The piecewise linear interface calculation is used to capture interfaces and perform accurate estimations of cell-edged density and viscosity. (3) The conservative Navier–Stokes equations are solved with the convective term discretized by a second and third order interpolation for convection scheme. (4) A fractional-step method is applied to solve the conservative Navier–Stokes equations, and the BiCGSTAB algorithm is used to solve the algebraic equations by discretizing the pressure-correction equation. The above features guarantee a simple, stable, efficient, and accurate simulation of two-phase flow problems. The effectiveness of the ADV-VOF method is verified by comparing it with the conventional volume of fluid method with rough treatment of cell-edged density and viscosity. It is found that the ADV-VOF method could successfully model the two-phase problems with large density ratio and viscosity ratio between two phases and is better than the conventional volume of fluid method in this respect. [DOI: 10.1115/1.4002981]

Keywords: ADV-VOF, IDV-VOF, two-phase flow, collocated grid system

1 Introduction

Flows with a spatial variation in fluid properties such as two-phase flows can be found in many natural phenomena and industrial facilities such as chemical reactors, power plants, and copper refining and internal combustion engines. The existence of vorticities and discontinued fluid properties produces complex flow structures, presenting the challenge to simulate these flows. Many methods have been proposed to simulate complex two-phase flows such as the front tracking method [1–4], the marker particle method [5,6], the level set (LS) method [7–9], and the volume of fluid (VOF) method [10–17]. The VOF method is a popular one, which can predict the complicated interface topology and fully guarantee the mass conservation while still maintaining a sharp representation of the interfaces.

In the VOF method, a volume fraction function C ranging from 0 to 1 is defined to denote whether the space is occupied by a dispersed phase or a continuous phase. When the value of C is unity, the space is occupied by the dispersed phase; when the value of C is zero, the space is occupied by the continuous phase; when the value of C is between 0 and 1, the space contains both the dispersed phase and the continuous phase, where an interface exists by definition. C is a step function, so it is difficult to calculate the accurate cell-edged density and viscosity, which is the reason why the VOF method easily gets divergent results.

To overcome this issue, the nonconservative Navier–Stokes equations are adopted [14,16,17], avoiding the appearance of cell-edged density in the convection term. However, solution by the nonconservative equations is not satisfied with the real physical nature of the studied problems [18]. The solution process becomes unstable with the large density ratio and the viscosity ratio between two phases.

In a general sense, the conservative Navier–Stokes equations compute problems accurately and stably [18]. The cell-edged density and viscosity have to be obtained in this case. For the traditional method, they are calculated by linear interpolation, which easily leads to large errors for two-phase flow problems. An example is given here, as shown in Fig. 1. The exact density at cell edge $(i+1/2,j)$ is equal to the continuous phase density ρ_c, but the density calculated by the linear interpolation is

$$(\rho_{i,j} + \rho_{i+1,j})/2 = \{[\rho_d \times C_{i,j} + \rho_c \times (1 - C_{i,j})] + \rho_c\}/2 \quad (1)$$

where the subscripts d and c denote the dispersed phase and the continuous phase, respectively. There is a large difference between the exact density and the calculated value by the linear interpolation. The inaccurate density and viscosity easily result in the divergence of the VOF method with the large density ratio and the viscosity ratio between two phases. We call the inaccurate density and viscosity volume of fluid method as IDV-VOF.

To decrease errors caused by the linear interpolation, Rudman [19] proposed the fine grid volume tracking (FGVT) method on two sets of grid systems, with the fine-grid system on which the volume faction function C is advected and the staggered coarse-grid system on which the velocity and pressure are solved. The accurate cell-edged density and viscosity are calculated by the data exchanges between the coarse- and fine-grid systems. In this method, four sets of grids are needed for a 2D two-phase flow problem.

The objective of this paper is to present an accurate density and viscosity volume of fluid method called ADV-VOF. The computations are performed on a collocated grid system, and only one set of grid is needed. Calculations of the accurate cell-edged density and viscosity become very simple. The method will be described as follows: The advantage of the method is verified by comparing that with the conventional VOF method.
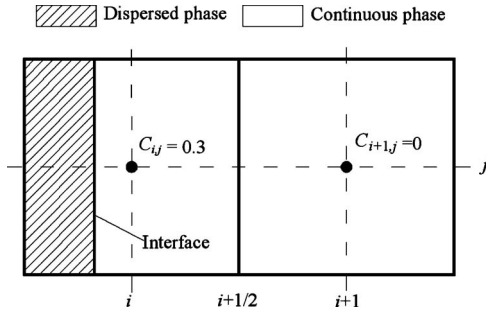
---

[1]Corresponding author.

Fig. 1 Distribution of dispersed phase, continuous phase, and their interface

2 ADV-VOF Method

To simplify the presentation, uniform grid is used with the two-dimensional Cartesian coordinates. Figure 2 shows the collocated grid system. Variables such as volume fraction function C, velocity $\boldsymbol{u}$, and pressure p are solved on one set of grid.

2.1 Governing Equations. In incompressible two-phase flows, both phases are described by a set of Navier–Stokes equations over the whole domain, which are written as follows: continuity equation

$$\nabla \cdot \boldsymbol{u}_f = 0 \tag{2}$$

momentum equation

$$\frac{\partial \rho \vec{u}}{\partial t} + \nabla \cdot (\rho_f \vec{u}_f \vec{u}) = -\nabla p + \nabla \cdot (\eta_f (\nabla \vec{u} + (\nabla \vec{u})^T)) + \rho \vec{g} + \vec{F} \tag{3}$$

The left side represents the transient term and the convective term, while the right side represents the pressure gradient, the viscous force, the body force, and the surface tension force.

In Eq. (3), the density ρ and dynamic viscosity η are evaluated by the volume faction function C expressed as

$$\frac{\partial C}{\partial t} + \nabla \cdot (\boldsymbol{u}_f C_f) = 0 \tag{4}$$

In Eqs. (2)–(4), variables with the subscript f refer to the cell-edged values, while variables without the subscript denote the cell-centered values.

2.2 Advection of Volume Fraction Function. The time-discretization form of Eq. (4) is written as

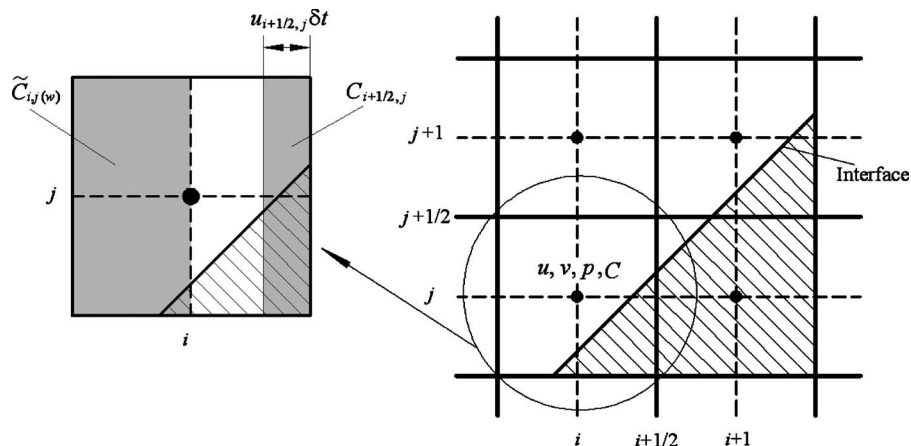$$C^{n+1} = C^n - \delta t \, \nabla \cdot (\boldsymbol{u}_f^n C_f^n) \tag{5}$$

To decrease errors induced by the mass residual, Eq. (5) is modified as

$$C^{n+1} = C^n - \delta t \, \nabla \cdot (\boldsymbol{u}_f^n C_f^n) + \delta t C^n \, \nabla \cdot (\boldsymbol{u}_f^n) \tag{6}$$

Equation (6) is solved by the VOF method in terms of the piece-wise linear interface calculation (PLIC) cited from Youngs [11].

We can obtain three types of volume fraction functions for the solution of Eq. (6). The first is the cell-centered volume fraction function C used to calculate the cell-centered density. The second is the cell-edged volume fraction function C_f obtained to evaluate the accurate cell-edged density. The right gray region at the cell (i,j) in Fig. 2 denotes the volume of the flux across the cell edge $(i+1/2,j)$. The oblique line in the gray region refers to the volume of the dispersed phase. The value of $C_{i+1/2,j}$ is equal to the ratio of the volume filled with the oblique lines over the volume of the gray region. The third is the half-cell volume fraction function $\widetilde{C}$ adopted to estimate the accurate cell-edged viscosity. As seen from Fig. 2, the left gray region at the cell (i,j) denotes a half volume, and the oblique lines in the gray region refer to the volume of the dispersed phase. The value of $\widetilde{C}_{i,j(w)}$ is equal to the ratio of the volume of the oblique lines over the volume of the gray region.

2.3 Density and Viscosity. For the transient term and the body force term in Eq. (3), the cell-centered density is expressed as

$$\rho = C\rho_d + (1 - C)\rho_c \tag{7}$$

For the convective term in Eq. (3), the accurate cell-edged density ρ_f is calculated based on the cell-edged volume fraction function C_f. For example, $\rho_{i+1/2,j}$ is computed as

$$\rho_{i+1/2,j} = C_{i+1/2,j}\rho_d + (1 - C_{i+1/2,j})\rho_c \tag{8}$$

For the viscous term in Eq. (3), the accuracy cell-edged viscosity η_f is evaluated in terms of the half-cell volume fraction function $\widetilde{C}$. For example, $\eta_{i+1/2,j}$ is computed as

$$\eta_{i+1/2,j} = \frac{2\,\widetilde{\eta}_{i,j(e)}\,\widetilde{\eta}_{i+1,j(w)}}{\widetilde{\eta}_{i,j(e)} + \widetilde{\eta}_{i+1,j(w)}} \tag{9}$$

where

$$\widetilde{\eta}_{i,j(e)} = \widetilde{C}_{i,j(e)}\eta_d + (1 - \widetilde{C}_{i,j(e)})\eta_c \tag{10}$$

$$\widetilde{\eta}_{i+1,j(w)} = \widetilde{C}_{i+1,j(w)}\eta_d + (1 - \widetilde{C}_{i+1,j(w)})\eta_c \tag{11}$$

Fig. 2 The collocated grid system and the relative variables

2.4 Discretization Schemes for the Convective and Viscous Terms.

To develop a computational program for the fluid flow and/or heat transfer, it is expected to adopt a modeling scheme with high accuracy, stability, and boundedness at a reasonable computational cost. Conflict exists between the accuracy and stability. Generally, a modeling scheme with high order accuracy may lead to unphysical oscillatory and/or overshoot/undershoot behavior in the region where steep gradients exist. On the other hand, the classical first order upwind scheme (FUS) or the like often suffer severe inaccuracies due to the so-called false diffusion induced by the low order truncation error. Obviously, high accuracy, stability, and boundedness are the important features to reasonably simulate two-phase problems, especially with large density ratio and viscosity ratio across the phase interface. In our study we adopt the second and third order interpolation for convection (STOIC) scheme [20] for the convective term in Eq. (3), which has been proved to be accurate, stable, and bounded.

In this paper, the viscous term in Eq. (3) is discretized by the central difference scheme, having the second order accuracy.

2.5 Surface Tension Force.

The surface tension force F in Eq. (3) is modeled using the continuum surface force (CSF) model developed by Brackbill et al. [21]. An interface is interpolated as a transient region with a finite thickness. The surface tension force located in this region is converted into a volume force with the help of a Dirac delta function, which is written as

$$F = \sigma \kappa \nabla C \qquad (12)$$

where σ and κ denote the surface tension coefficient and the curvature of interfaces, respectively.

The curvature is obtained from

$$\kappa = -(\nabla \cdot \mathbf{n}) \qquad (13)$$

Equation (13) can be recast into

$$\kappa = \frac{1}{|\mathbf{n}|}\left[\left(\frac{\mathbf{n}}{|\mathbf{n}|}\cdot\nabla\right)|\mathbf{n}| - (\nabla\cdot\mathbf{n})\right] \qquad (14)$$

which can give better results in practice [21]. In Eqs. (13) and (14), the unit normal vector to a surface is defined by

$$\mathbf{n} = \frac{\nabla\hat{C}}{|\nabla\hat{C}|} \qquad (15)$$

where $\hat{C}$ is a smoothed volume fraction function, which improves the accuracy of curvature, coming from

$$\hat{C}_{i,j} = \sum_{m,n} C_{m,n}K(|\mathbf{r}_{i,j} - \mathbf{r}_{m,n}|,h)\,\delta x\,\delta y \qquad (16)$$

where the smoothening function K is given by the cubic B-spline proposed by Monaghan [22],

$$K(r,h) = \begin{cases} \dfrac{40}{7\pi}\left(1 - 6\left(\dfrac{r}{h}\right)^2 + 6\left(\dfrac{r}{h}\right)^3\right) & \text{if } \dfrac{r}{h} < \dfrac{1}{2} \\[2mm] \dfrac{80}{7\pi}\left(1 - \dfrac{r}{h}\right)^3 & \text{if } \dfrac{r}{h} < 1 \\[2mm] 0 & \text{otherwise} \end{cases} \qquad (17)$$

where h represents the width of the computational stencil used for smoothening. Typically, we use $h = 3\Delta$ where Δ represents the grid size. The width of the computational stencil for the smoothening should be selected carefully. If the width is too small, then the curvature accuracy is low, causing numerical instabilities. If the width of the computational stencil is too large, then we achieve an excessive smoothening and cannot capture a small change of the curvature.

2.6 Time Integration.

In Secs. 2.3–2.5, the methods to compute the density, viscosity, convective term, viscous term, and surface tension force in Eq. (3) are described. In this section, we solve the time dependent incompressible Navier–Stokes equations on a collocated grid system. The fractional-step method [23,24] is used. The crucial issue of the method is to eliminate the decoupling between pressure and velocity. The momentum interpolation method (MIM) was proposed to avoid the decoupling on the collocated grid system in 1980s [25], which is incorporated with the fractional-step method here.

Now we describe the fractional-step method. The intermediate cell-centered velocity is obtained as follows:

$$\mathbf{u}^* = \frac{\delta t}{\rho^{n+1}}\left[-\nabla\cdot(\rho_f\mathbf{u}_f\mathbf{u}) + \nabla\cdot(\eta_f(\nabla\mathbf{u} + (\nabla\mathbf{u})^T)) + \rho\mathbf{g} + \frac{\rho\mathbf{u}}{\delta t}\right]^n$$
$$+ \frac{\delta t}{\rho^{n+1}}[\sigma\kappa\nabla C]^n - \frac{\delta t}{\rho^{n+1}}[\nabla p]^n \qquad (18)$$

Equation (18) is the time-discretization form of Eq. (3). We define the following:

$$\tilde{\mathbf{u}} = \frac{\delta t}{\rho^{n+1}}\left[-\nabla\cdot(\rho_f\mathbf{u}_f\mathbf{u}) + \nabla\cdot(\eta_f(\nabla\mathbf{u} + (\nabla\mathbf{u})^T)) + \rho\mathbf{g} + \frac{\rho\mathbf{u}}{\delta t}\right]^n \qquad (19)$$

$$D = \frac{\delta t}{\rho^{n+1}} \qquad (20)$$

Then, we have

$$\mathbf{u}^* = \tilde{\mathbf{u}} + D[\sigma\kappa\nabla C]^n - D[\nabla p]^n \qquad (21)$$

The u,v-component in Eq. (21) is written as

$$u^*_{i,j} = \tilde{u}_{i,j} + D_{i,j}\left[\sigma\kappa\frac{\partial C}{\partial x}\right]^n_{i,j} - D_{i,j}\left[\frac{\partial p}{\partial x}\right]^n_{i,j} \qquad (22)$$

$$v^*_{i,j} = \tilde{v}_{i,j} + D_{i,j}\left[\sigma\kappa\frac{\partial C}{\partial y}\right]^n_{i,j} - D_{i,j}\left[\frac{\partial p}{\partial y}\right]^n_{i,j} \qquad (23)$$

where

$$\left[\frac{\partial C}{\partial x}\right]_{i,j} = \frac{C_{i+1,j} - C_{i-1,j}}{2\delta x}, \quad \left[\frac{\partial C}{\partial y}\right]_{i,j} \frac{C_{i,j+1} - C_{i,j-1}}{2\delta y} \qquad (24)$$

$$\left[\frac{\partial p}{\partial x}\right]_{i,j} = \frac{p_{i+1,j} - p_{i-1,j}}{2\delta x}, \quad \left[\frac{\partial p}{\partial y}\right]_{i,j} = \frac{p_{i,j+1} - p_{i,j-1}}{2\delta y} \qquad (25)$$

We express the intermediate cell-edged velocity by mimicking Eq. (21) as

$$\mathbf{u}^*_f = \tilde{\mathbf{u}}_f + D_f[\sigma\kappa\nabla C]^n_f - D_f[\nabla p]^n_f \qquad (26)$$

The u,v-component in Eq. (26) is written as

$$u^*_{i+1/2,j} = \tilde{u}_{i+1/2,j} + D_{i+1/2,j}\left[\sigma\kappa\frac{\partial C}{\partial x}\right]^n_{i+1/2,j} - D_{i+1/2,j}\left[\frac{\partial p}{\partial x}\right]^n_{i+1/2,j} \qquad (27)$$

$$v^*_{i,j+1/2} = \tilde{v}_{i,j+1/2} + D_{i,j+1/2}\left[\sigma\kappa\frac{\partial C}{\partial y}\right]^n_{i,j+1/2} - D_{i,j+1/2}\left[\frac{\partial p}{\partial y}\right]^n_{i,j+1/2} \qquad (28)$$

where

$$\tilde{u}_{i+1/2,j} = (\tilde{u}_{i,j} + \tilde{u}_{i+1,j})/2, \quad \tilde{v}_{i,j+1/2} = (\tilde{v}_{i,j} + \tilde{v}_{i,j+1})/2 \qquad (29)$$

$$D_{i+1/2,j} = (D_{i,j} + D_{i+1,j})/2, \quad D_{i,j+1/2} = (D_{i,j} + D_{i,j+1})/2 \qquad (30)$$

$$\kappa_{i+1/2,j} = (\kappa_{i,j} + \kappa_{i+1,j})/2, \quad \kappa_{i,j+1/2} = (\kappa_{i,j} + \kappa_{i,j+1})/2 \qquad (31)$$

$$\left[\frac{\partial C}{\partial x}\right]_{i+1/2,j} = \frac{C_{i+1,j} - C_{i,j}}{\delta x}, \quad \left[\frac{\partial C}{\partial y}\right]_{i,j+1/2} = \frac{C_{i,j+1} - C_{i,j}}{\delta y} \qquad (32)$$

$$\left[\frac{\partial p}{\partial x}\right]_{i+1/2,j} = \frac{p_{i+1,j} - p_{i,j}}{\delta x}, \quad \left[\frac{\partial p}{\partial y}\right]_{i,j+1/2} = \frac{p_{i,j+1} - p_{i,j}}{\delta y} \quad (33)$$

The intermediate cell-edged velocity $\boldsymbol{u}_f^*$ expressed in Eq. (26) satisfies the momentum equation but cannot satisfy the mass conservation condition. The pressure and the intermediate cell-edged velocity should be modified so that the updated cell-edged velocity satisfies the continuity equation. The following Poisson equation for the pressure correction p' is solved to obtain an improved cell-edged velocity field,

$$\nabla \cdot [D_f(\nabla p')_f] = -\nabla \cdot (\boldsymbol{u}_f^*) \quad (34)$$

The improved pressure and the cell-edged and cell-centered velocities are

$$p^{n+1} = p^n + p' \quad (35)$$

$$\boldsymbol{u}_f^{n+1} = \boldsymbol{u}_f^* - D_f[\nabla p']_f \quad (36)$$

$$\boldsymbol{u}^{n+1} = \boldsymbol{u}^* - D[\nabla p'] \quad (37)$$

2.7 Pressure Correction Solution. The pressure-correction equation (Eq. (34)) is solved using a robust and efficient BiCG-STAB algorithm proposed by van der Vorst [26,27]. The discretization form of the equation is

$$a_P p_P' = a_E p_E' + a_W p_W' + a_N p_N' + a_S p_S' + b \quad (38)$$

where

$$a_E = \frac{D_e}{\delta x}, \quad a_W = \frac{D_w}{\delta x}, \quad a_N = \frac{D_n}{\delta y}, \quad a_S = \frac{D_s}{\delta y} \quad (39)$$

$$a_P = a_E + a_W + a_N + a_S \quad (40)$$

$$b = u_w^* - u_e^* + v_s^* - v_n^* \quad (41)$$

In Eqs. (38)–(41), the subscripts—P, E, W, N, and S—denote the cell centers (i,j), $(i+1,j)$, $(i-1,j)$, $(i,j+1)$, and $(i,j-1)$; e, w, n, and s refer to the cell edges $(i+1/2,j)$, $(i-1/2,j)$, $(i,j+1/2)$, and $(i,j-1/2)$, respectively.

The matrix form of Eq. (38) is

$$\underline{A}\boldsymbol{p}' = \boldsymbol{B} \quad (42)$$

where the matrix $\underline{A}$ is expressed as

$$\underline{A} = \begin{pmatrix} 0 & A^N & 0 \\ & A^E & \\ 0 & A^W & A^P & 0 \\ A^S & & \\ 0 & & 0 \end{pmatrix} \quad (43)$$

In Eq. (43), the five nonzero diagonals A^P, A^E, A^W, A^N, and A^S consist of the coefficients a_P, $-a_E$, $-a_W$, $-a_N$, and $-a_S$. The matrix $\underline{A}$ is rewritten as

$$\text{entry}(\underline{A}) = (A^S, A^W, A^P, A^E, A^N) \quad (44)$$

We use the MILU method [28] to precondition the matrix $\underline{A}$. The preconditioner $\underline{M}$ is defined as

$$\underline{M} = \underline{L}\underline{D}\underline{U} \quad (45)$$

The matrix entries of $\underline{L}$, $\underline{D}$, and $\underline{U}$ are written as

$$\text{entry}(\underline{L}) = \left(A^S, A^W, \frac{1}{D^P}, 0, 0\right)$$

$$\text{entry}(\underline{D}) = (0,0,D^P,0,0)$$

$$\text{entry}(\underline{U}) = \left(0,0,\frac{1}{D^P},A^E,A^N\right) \quad (46)$$

where D^P is computed as

$$D_{i,j}^P = \frac{1}{A_{i,j}^P - D_{i-1,j}^P A_{i,j}^W(A_{i-1,j}^E + \alpha A_{i-1,j}^N) - D_{i,j-1}^P A_{i,j}^S(A_{i,j-1}^N + \alpha A_{i,j-1}^E)} \quad (47)$$

where α is set to be 0.99.

Based on the preconditioner $\underline{M}$, the procedure of the BiCG-STAB algorithm to solve Eq. (42) is as follows:

Step 1. Set $\boldsymbol{p}'^0$ as an initial vector,

$$\boldsymbol{r}^0 = \boldsymbol{B} - \underline{A}\boldsymbol{p}'^0$$

Step 2. Set $\boldsymbol{r}'$ as an arbitrary vector such that $(\boldsymbol{r}',\boldsymbol{r}^0) \neq 0$; e.g., $\boldsymbol{r}' = \boldsymbol{r}^0$,

$$\phi^0 = \chi = \omega^0 = 1, \quad \boldsymbol{w}^0 = \boldsymbol{q}^0 = 0$$

Step 3. For $k=1,2,\ldots$ until $\boldsymbol{r}^k <$ tolerance,

$$\phi^k = (\boldsymbol{r}',\boldsymbol{r}^{k-1}), \quad \beta = (\phi^k/\phi^{k-1})/(\chi/\omega^{k-1}),$$

$$\boldsymbol{q}^k = \boldsymbol{r}^{k-1} + \beta(\boldsymbol{q}^{k-1} - \omega^{k-1}\boldsymbol{w}^{k-1})$$

Solve $\boldsymbol{y}$ from $\underline{M}\boldsymbol{y} = \boldsymbol{q}^k$; $\boldsymbol{w}^k = \underline{A}\boldsymbol{y}$

$$\chi = \phi^k/(\boldsymbol{r}',\boldsymbol{w}^k), \quad \boldsymbol{s} = \boldsymbol{r}^{k-1} - \chi\boldsymbol{w}^k$$

Solve $\boldsymbol{z}$ from $\underline{M}\boldsymbol{z} = \boldsymbol{s}$; $\boldsymbol{t} = \underline{A}\boldsymbol{z}$

$$\omega^k = (\boldsymbol{t},\boldsymbol{s})/(\boldsymbol{t},\boldsymbol{t})$$

Then the new vector is $\boldsymbol{p}'^k = \boldsymbol{p}'^{k-1} + \chi\boldsymbol{y} + \omega^k\boldsymbol{z}$,

$$\boldsymbol{r}^k = \boldsymbol{s} - \omega^k\boldsymbol{t}$$

2.8 Solution Procedure of ADV-VOF Method. *Step 1.* Advect the volume fraction function Eq. (4) by adopting the VOF method based on the piecewise linear interface calculation (Sec. 2.2).

Step 2. Calculate the cell-centered and cell-edged densities and the viscosity in Eq. (3) (Sec. 2.3).

Step 3. Solve the Navier–Stokes equations (Eqs. (2) and (3)) using the fractional-step method (Sec. 2.6).

3 Numerical Comparisons

The objective of this section is to verify the advantage of the ADV-VOF method by comparing it with the IDV-VOF method via three two-phase flow problems.

3.1 The Dam Break Problem. Figure 3 shows the physical model of the dam break problem. The initial liquid column has a width of 0.146 m and a height of 0.292 m. The physical properties are liquid density $\rho_l = 1.0 \times 10^3$ kg/m^3, viscosity $\mu_l = 0.5$ Pa s, background gas density $\rho_g = 1.0$ kg/m^3, viscosity $\mu_g = 0.5 \times 10^{-3}$ Pa s, gravity $g = 9.8$ m/s^2, and surface tension coefficient $\sigma = 0.0755$ N/m. Thus, both the density ratio and the viscosity ratio of liquid over gas are 1000:1. Calculations are performed for two different computational grids 80×80 and 120×120 with the no-slip boundary condition.

Figure 4 shows the results computed by the ADV-VOF method for two different computational grids and those reported by Martin and Moyce [29]. The present numerical results are fully converged and agree with the experimental data very well, proving that the ADV-VOF method can get accurate solutions with the large density ratio and the viscosity ratio. However, the IDV-VOF method cannot reach convergent solutions in this case.

3.2 The Droplet Falling Problem. The droplet falling problem is studied here. A liquid droplet of 0.01 m in diameter is released from position (0.025 m, 0.15 m) in an initially quiescent gas. The domain size is 0.05×0.2 m^2, with free slip boundary
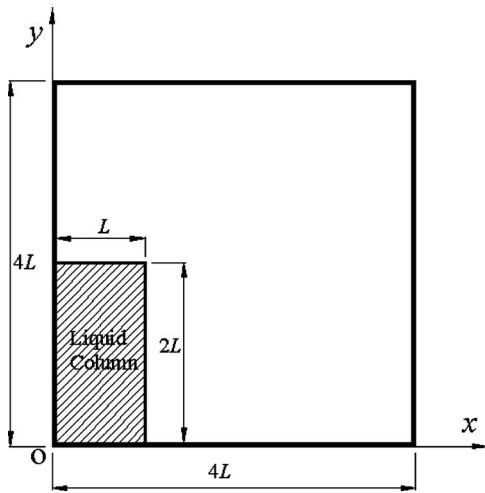
Fig. 3 Physical model of dam break problem

Fig. 6 Droplet falling velocity with time

condition on the walls. The liquid droplet density $\rho_l = 1.0 \times 10^3$ kg/m^3, viscosity $\mu_l = 0.01$ Pa s, gravity $g = 9.8$ m/s^2, and surface tension coefficient $\sigma = 0.01$ N/m. The density ratio and the viscosity ratio are the same, and their values are set to be 10:1, 100:1, 1000:1, and 10,000:1, respectively.

In order to show the effects of grid refinement, the calculation is carried out on the computational grids 50×200, 75×300, and 100×400. In Fig. 5, we compare the droplet shapes at $t = 0.1$ s. There is little difference for the droplet shapes when the computation grids are equal to 75×300 and 100×400. So we select 75×300 as the computational grid in this problem.

Figure 6 shows the theoretical solutions of the droplet falling velocity without gas drag force (i.e., $v = gt$); the results computed by the ADV-VOF method are at the ratios 10:1, 100:1, 1000:1, and 10,000:1, and the results calculated by the IDV-VOF method
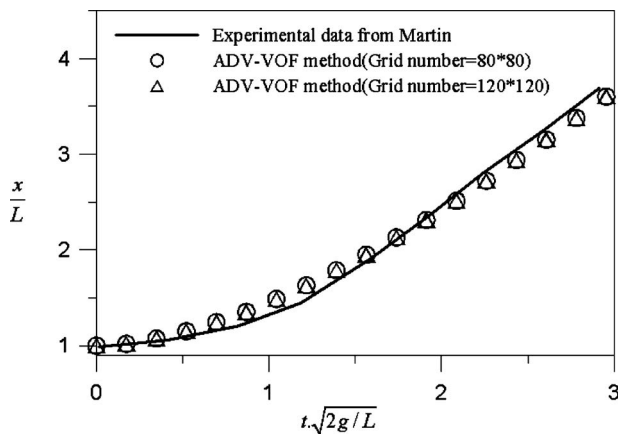
are at the ratio 10:1. It is found that the droplet falling velocity gradually approaches the theoretical solutions with increases in the density ratio and the viscosity ratio. When the density and viscosity ratios are 10,000:1, the gas drag force is almost negligible; the droplet falling velocity approaches the theoretical solutions. It is proved that the ADV-VOF method is accurate. The ADV-VOF method obtains convergent solutions at the ratios 10:1, 100:1, 1000:1, and 10,000:1, but the IDV-VOF method only reaches convergent results at the ratio 10:1. The above difference of the two methods is caused by the different treatments of the cell-edged density and viscosity. In the ADV-VOF method, the accurate cell-edged density and viscosity are evaluated by the PLIC, but in the IDV-VOF method, the cell-edged density and viscosity are estimated by the linear interpolation, which causes large errors.

Figure 7 shows the droplet falling velocity fields based on the ADV-VOF and IDV-VOF methods at the ratio of 100:1. Reasonable results are obtained by the ADV-VOF method, but results by the IDV-VOF method are not reasonable due to the divergent solution of the method at the large density and viscosity ratios of 100:1.

Fig. 4 History of fluid front marching along the ground surface
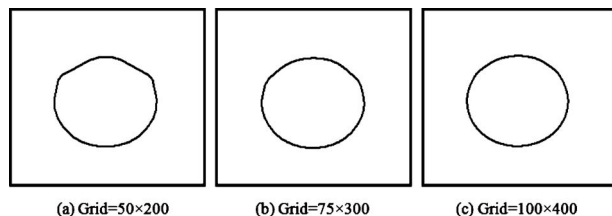
Fig. 5 Droplet shapes at $t = 0.1$ s at the ratio 1000:1

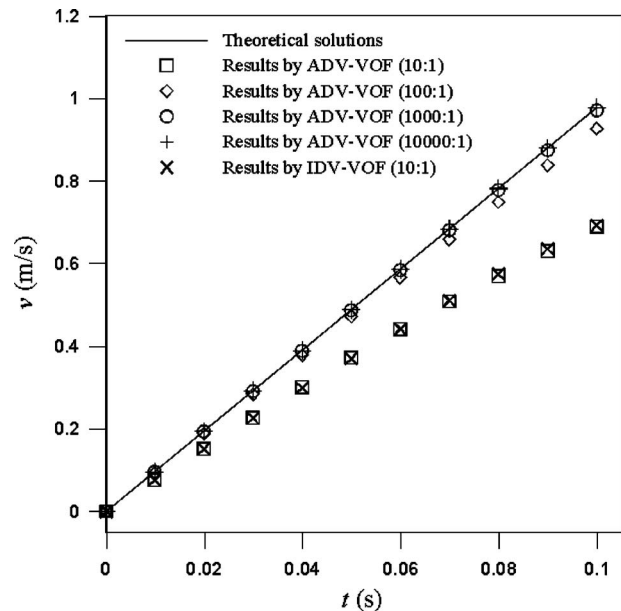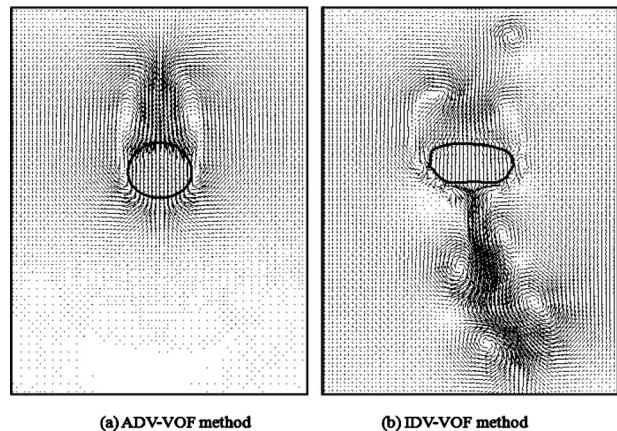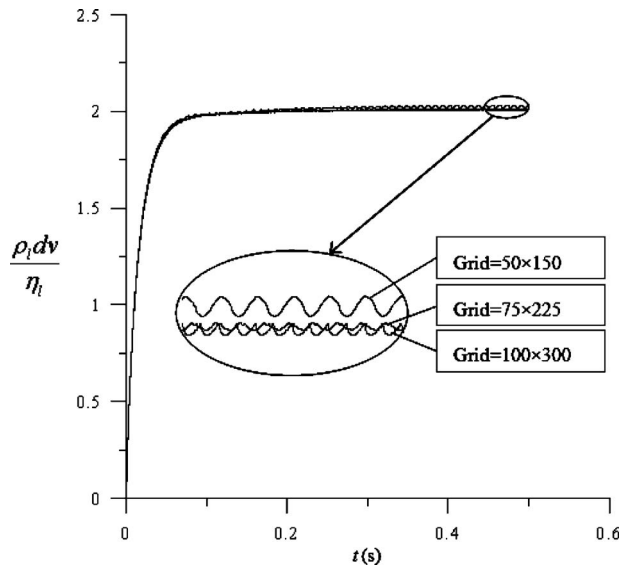Fig. 7 Droplet falling velocity field at the ratio 100:1 computed by the ADV-VOF and IDV-VOF methods

Fig. 8 Rising velocity of the single gas bubble with time for case 3 at the ratio 1000:1

3.3 Single Gas Bubble Rising Problem. Grace [30] analyzed a large amount of experimental data on a single gas bubble rising in an infinite quiescent liquid. He concluded that the single gas bubble's rising performance is determined by four independent dimensionless parameters: the Morton number (M), the Eotvos number (Eo), the viscosity ratio (κ), and the density ratio (γ), which are defined as

$$M = g \eta_l^4 / \rho_l \sigma^3 \qquad (48)$$

$$Eo = g d^2 (\rho_l - \rho_g)/\sigma \qquad (49)$$

$$\gamma = \rho_l / \rho_g \qquad (50)$$

$$\lambda = \eta_l / \eta_g \qquad (51)$$

where d is the initial bubble diameter. It is sufficient to consider only two dimensionless groups (M and Eo) when both γ and λ tend to be very large [30], because in this situation, gas has little influence on the bubble properties such as the bubble terminal shapes and the Reynolds number (Re). The bubble Reynolds number Re is defined as

$$Re = \rho_l d v_\infty / \eta_l \qquad (52)$$

where v_∞ is the terminal bubble rising velocity.

A single gas bubble with diameter $d=0.01$ m is released from the position (0.025 m, 0.02 m) in a quiescent liquid. The domain size is 0.05×0.15 m^2, with free slip boundary condition on the walls. Three cases are studied: Eo=1.0 and M=0.001 for case 1, Eo=10.0 and M=0.1 for case 2, and Eo=100.0 and M=1000.0 for case 3. In the three cases, the density ratio and the viscosity ratio of $\gamma=\lambda=100:1$ and $\gamma=\lambda=1000:1$ are adopted, which are sufficiently large to have little influence on the bubble properties.

For evaluating the grid independent, three different computational grids (50×150, 75×225, and 100×300) are adopted to calculate the rising velocity of the single gas bubble with time for case 3. As shown in Fig. 8, there is little difference for the rising velocity when the computation grids are equal to 75×225 and 100×300. So we select 75×225 as the computational grid in this problem.

Figure 9 shows the bubble terminal shapes of the three cases computed by the ADV-VOF method, which are spherical for case 1, ellipsoidal for case 2, and spherical-cap for case 3. The computed bubble shapes are exactly the same as the experimental
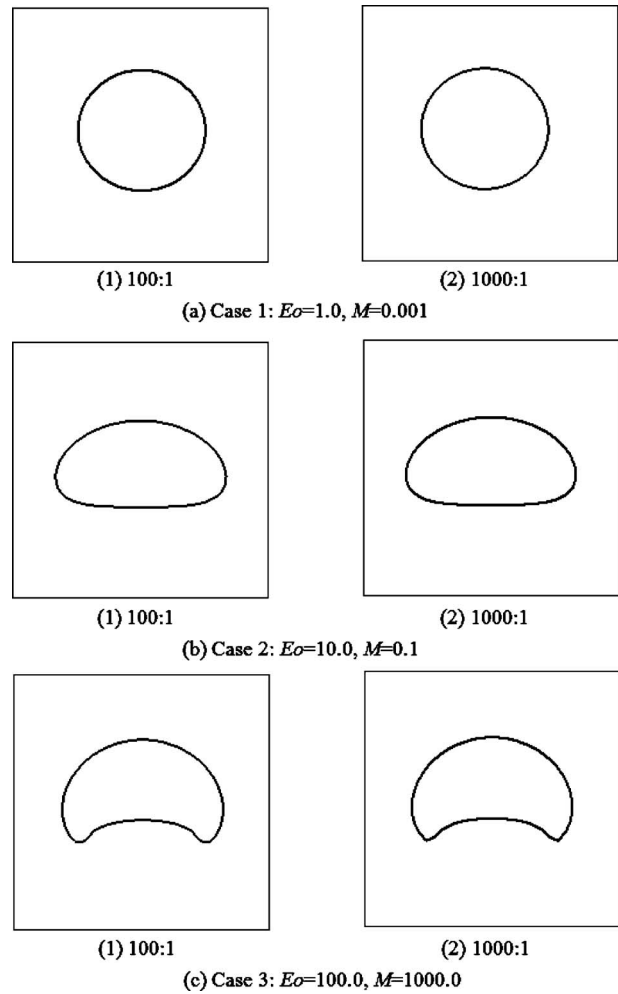

Fig. 9 Bubble terminal shapes computed by the ADV-VOF method

observations reported by Grace [30]. It is seen from Fig. 9 and Table 1 that the bubble terminal shapes and Re, computed by the ADV-VOF method, are slightly different for the two density and viscosity ratios of 100:1 and 1000:1. It is found from Table 1 that the ADV-VOF method reaches convergent solutions at the ratios of 100:1 and 1000:1, but the IDV-VOF method can only achieve convergent solutions at the ratio of 100:1. The IDV-VOF method is not convergent due to large errors of the cell-edged density and viscosity at the density and viscosity ratios of 1000:1.

Incorporating the above three problems studied, it is concluded that the ADV-VOF method is greatly superior to the IDV-VOF method under the large density and viscosity ratios between the two phases.

Sussman et al. [31] and Kang et al. [32] used height fraction to calculate the cell-edged density and viscosity. In these two references, the nonconservative Navier–Stokes equations are adopted,

Table 1 Reynolds number (Re) computed by the ADV-VOF and IDV-VOF methods

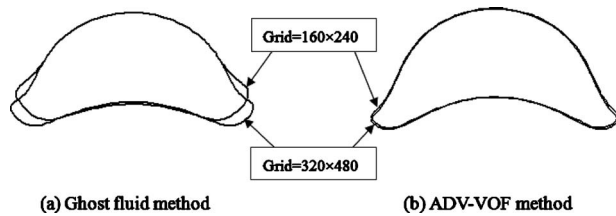| Method	ADV-VOF		IDV-VOF	
Ratio	100:1	1000:1	100:1	1000:1
Re (Case 1)	2.548	2.548	2.526	Divergence
Re (Case 2)	4.765	4.797	4.726	Divergence
Re (Case 3)	1.999	2.010	1.973	Divergence

Fig. 10 Air bubble shapes at $t=0.05$ s on the computational grids 160×240 and 320×480

avoiding the appearance of the cell-edged density in the convection term, so the cell-edged density refers to the average density of the fluid in the control volume of the cell-edged velocity. In the ADV-VOF method, the conservative Navier–Stokes equations are applied, so the cell-edged density denotes the average density of the fluid across the cell edge. Generally, the conservative Navier–Stokes equations compute problems more accurately. Here, the problem of the single air bubble rising in quiescent water is used to compare the ADV-VOF method with the ghost fluid method reported by Kang et al. [32]. The physical properties are $\rho_{\text{water}}=1.0\times10^3$ kg/m^3, $\mu_{\text{water}}=1.137\times10^{-3}$ Pa s, $\rho_{\text{air}}=1.226$ kg/m^3, $\mu_{\text{air}}=1.78\times10^{-5}$ Pa s, $g=9.8$ m/s^2, and $\sigma=0.0728$ N/m. The domain size is 0.02×0.03 m^2, with free slip boundary condition on the walls. A circular air bubble with a radius of 1/300 m is released from the position (0.01 m, 0.01 m) in quiescent water. Figure 10 shows the air bubble shapes at $t=0.05$ s on the different computational grids 160×240 and 320×480, which are calculated by the ADV-VOF method and the ghost fluid method, respectively. As shown in this figure, the variation in the computational grid has little influence on the air bubble shapes for the ADV-VOF method; however, the influence is large for the ghost fluid method. The ADV-VOF method shows its superiority in this aspect.

4 Conclusions

In this paper, the ADV-VOF method is proposed to solve two-phase flow problems on the collocated grid system, which is a simple, stable, efficient, and accurate method.

The simplicity of the method is ensured by the following: (1) The variables of the volume fraction function, velocity, and pressure are solved on one set of the grid. (2) The accurate cell-edged density and viscosity are evaluated on the collocated grid system.

The stability and accuracy of the method are ensured by the following: (1) The conservative Navier–Stokes equations are adopted and the accurate cell-edged density and viscosity are calculated. (2) A STOIC scheme, having high accuracy, stability, and boundedness, is applied for the convection term.

The computation efficiency is described as follows: (1) The fractional-step method is applied to solve the conservative Navier–Stokes equations. (2) The BiCGSTAB algorithm is adopted to solve the algebraic equations formed by discretizing the pressure-correction equation.

The effectiveness of the ADV-VOF method is verified by comparing that with the IDV-VOF method. It is concluded that the ADV-VOF method is greatly superior to the IDV-VOF method. The proposed new method obtains accurate, stable, and convergent solutions with large density and viscosity ratios between the two phases.

Acknowledgment

Nomenclature

a = coefficient in the discretized equation
$\underline{A}$ = coefficient matrix
A^P, A^E, A^W, A^N, A^S = five nonzero diagonals of coefficient matrix $\underline{A}$
b = constant term in the discretized equation
C = volume fraction function
$\hat{C}$ = smoothed volume fraction function
d = initial bubble diameter
Eo = Eotvos number
$\boldsymbol{F}$ = surface tension force
g = gravity
h = width of the computational stencil
K = smoothening function
M = Morton number
$\underline{M}$ = preconditioner
$\boldsymbol{n}$ = unit normal vector
p = pressure
p' = pressure correction
r = distance
$\boldsymbol{r}$ = position vector; residual vector
t = time
u, v = velocity component in x, y directions
$\boldsymbol{u}$ = velocity vector
x, y = coordinates

Greek Symbols

γ = density ratio
η = dynamic viscosity
κ = interface curvature
λ = viscosity ratio
ρ = density
σ = surface tension coefficient

Subscripts

c = continuous phase
d = dispersed phase
e, w, n, s = cell edges
f = cell edge
g = gas phase
l = liquid phase
P, E, N, S, W = cell centers

Superscripts

n = time level
$*$ = intermediate value

References

[1] Unverdi, S. O., and Tryggvason, G., 1992, "A Front-Tracking Method for Viscous, Incompressible Multi-Fluid Flows," J. Comput. Phys., **100**, pp. 25–37.
[2] Esmaeeli, A., and Tryggvason, G., 1998, "Direct Numerical Simulation of Bubble Flows Part I. Low Reynolds Number Arrays," J. Fluid Mech., **377**, pp. 313–345.
[3] Esmaeeli, A., and Tryggvason, G., 1999, "Direct Numerical Simulation of Bubble Flows Part II. Moderate Reynolds Number Arrays," J. Fluid Mech., **385**, pp. 325–358.
[4] Tryggvason, G., Bunner, B., and Esmaeeli, A., 2001, "A Front Tracking Method for the Computations of Multiphase Flow," J. Comput. Phys., **169**(2), pp. 708–759.
[5] Welch, J. E., Harlow, F. H., Shannon, J. P., and Daly, B. J., 1965, "The MAC Method: A Computing Technique for Solving Viscous Incompressible Transient Fluid Flow Problems Involving Free Surfaces," Los Alamos Scientific Laboratory, Report No. LA-3425.
[6] Rider, W. J., and Kothe, D. B., 1995, "Stretching and Tearing Interface Tracking Methods," http://laws.lanl.gov/XHM/personnel/wjr/Web_papers/pubs.html
[7] Sussman, M., Smereka, P., and Osher, S., 1994, "A Level Set Approach for Computing Solutions to Incompressible Two-Phase Flow," J. Comput. Phys., **114**, pp. 146–159.
[8] Son, G., and Dhir, V. K., 1998, "Numerical Simulation of Film Boiling Near Critical Pressures With a Level Set Method," ASME J. Heat Transfer, **120**, pp. 183–192.
[9] Osher, S., and Fedkiw, R. P., 2001, "Level Set Methods: An Overview and Some Recent Results," J. Comput. Phys., **169**, pp. 463–502.

[10] Hirt, C. W., and Nichols, B. D., 1981, "Volume of Fluid (VOF) Method for the Dynamics of Free Boundary," J. Comput. Phys., **39**, pp. 201–225.

[11] Youngs, D. L., 1982, *Time-Dependent Multi-Material Flow With Large Fluid Distortion Numerical Method for Fluid Dynamics*, Academic, New York, pp. 273–285.

[12] Rider, W. J., and Kothe, D. B., 1998, "Reconstructing Volume Tracking," J. Comput. Phys., **141**, pp. 112–152.

[13] Chen, L., and Li, Y. G., 1998, "A Numerical Method for Two-Phase Flows With an Interface," Environ. Modell. Software, **13**, pp. 247–255.

[14] Gueyffier, D., Li, J., Nadim, A., Scardovelli, R., and Zaleski, S., 1999, "Volume-of-Fluid Interface Tracking With Smoothed Surface Stress Methods for Three-Dimensional Flows," J. Comput. Phys., **152**, pp. 423–456.

[15] Agarwal, D. K., Welch, S. W. J., Biswas, G., and Durst, F., 2004, "Planar Simulation of Bubble Growth in Film Boiling in Near-Critical Water Using a Variant of the VOF Method," ASME J. Heat Transfer, **126**, pp. 329–338.

[16] Ginzburg, I., and Wittum, G., 2001, "Two-Phase Flows on Interface Refined Grids Modeled With VOF, Staggered Finite Volume, and Spline Interpolants," J. Comput. Phys., **166**, pp. 302–335.

[17] Lorstad, D., and Fuchs, L., 2004, "High-Order Surface Tension VOF-Model for 3D Bubble Flows With High Density Ratio," J. Comput. Phys., **200**, pp. 153–176.

[18] Tao, W. Q., 2001, *Numerical Heat Transfer*, 2nd ed., Xi'an Jiaotong University Press, Xi'an, Shaanxi, P.R. China.

[19] Rudman, M., 1998, "A Volume-Tracking Method for Incompressible Multi-fluid Flows With Large Density Variations," Int. J. Numer. Methods Fluids, **28**, pp. 357–378.

[20] Darwish, M. S., 1993, "A New-High Resolution Scheme Based on the Normalized Variable Formulation," Numer. Heat Transfer, Part B, **24**, pp. 353–371.

[21] Brackbill, J. U., Kothe, D. B., and Zemach, C., 1992, "A Continuum Method for Modeling Surface Tension," J. Comput. Phys., **100**, pp. 335–354.

[22] Monaghan, J. J., 1992, "Smoothed Particle Hydrodynamics," Annu. Rev. Astron. Astrophys., **30**, pp. 543–574.

[23] Chorin, A. J., 1968, "Numerical Solution of the Navier–Stokes Equations," Math. Comput., **22**, pp. 745–762.

[24] Perot, J. B., 1993, "An Analysis of the Fractional Step Method," J. Comput. Phys., **108**, pp. 51–58.

[25] Rhie, C. M., and Chow, W. L., 1983, "Numerical Study of the Turbulent Flow Past an Airfoil With Trading Edge Separations," AIAA J., **21**(11), pp. 1525–1532.

[26] van der Vorst, H. A., 1992, "BI-CGSTAB: A Fast and Smoothly Converging Variant of BI-CG for the Solution of Nonsymmetric Linear Systems," SIAM (Soc. Ind. Appl. Math.) J. Sci. Stat. Comput., **13**(2), pp. 631–644.

[27] van der Vorst, H. A., 2002, "Efficient and Reliable Iterative Methods for Linear Systems," J. Comput. Appl. Math., **149**, pp. 251–265.

[28] Gustafsson, I., 1978, "A Class of First Order Factorization Methods," BIT, **18**, pp. 142–156.

[29] Martin, J. C., and Moyce, W. J., 1952, "An Experimental Study of the Collapse of Fluid Columns on a Rigid Horizontal Plane," Philos. Trans. R. Soc. London, Ser. A, **244**(882), pp. 312–324.

[30] Grace, J. R., 1973, "Shapes and Velocities of Bubbles Rising in Infinite Liquids," Trans. Inst. Chem. Eng., **51**, pp. 116–120.

[31] Sussman, M., Smith, K. M., Hussaini, M. Y., Ohta, M., and Zhi-Wei, R., 2007, "A Sharp Interface Method for Incompressible Two-Phase Flows," J. Comput. Phys., **221**, pp. 469–505.

[32] Kang, M., Fedkiw, R. P., and Liu, X. D., 2000, "A Boundary Condition Capturing Method for Multiphase Incompressible Flow," J. Sci. Comput., **15**(3), pp. 323–360.